# HIGH-FLEXIBILITY THREE-DIMENSIONAL SERIAL FOLDED HINGES

NICOLAE LOBONTIU , MORGAN MOSES, JOZEF HUNTER

*Abstract*. A new three-dimensional flexible hinge capable of large, linear-domain displacements is proposed for extended spatial workspace mechanisms. The hinge structure is compact and modular consisting of a large number of circular- and straight-axis segments connected in series and disposed in two parallel planes in a folded manner. The analytical, linear-model compliance matrix, which is necessary in direct/inverse kinematics and controls analysis, is derived based on simplified hinge geometry and small-deformation theory. The compliance model is accurate, as demonstrated by finite element simulation and experimental testing of a prototype. The compliance model is also utilized to determine the hinge piston-motion stiffness and the static response of several hinges connected in series. Another analytical compliance model is formulated to predict the hinge maximum loads and displacements in terms of allowable stresses. The mathematical models are further utilized to comprehensively investigate the influence of geometric parameters on the hinge performance.

*Key words:* flexible hinge, linear model, analytic, compliance, displacement, load, stress.

## 1. INTRODUCTION

Flexure/flexible hinges have widely been implemented as elastic joints in mechanisms of monolithic structure. Engineering applications that employ flexure hinges and their mechanisms are numerous and cover a wide and varied domain in the auto/aero, medical, computer industries, as well as in telecommunications, electronics or robotics. Actuators, sensors, flexible bearings, couplings and suspensions, airbags, endoprostheses, catheters, precision positioning devices in (laser) optics and microscopy, cameras, scanners or micro/nano electro-mechanical devices are just a few practical examples where flexure hinges are utilized.

Flexure hinges, such as the circular design of Fig. 1a, are primarily intended to bend (or flex) around a single axis and therefore enable the relative rotation between two adjacent rigid links. All other deformations (axial- or torsion-related)

University of Alaska Anchorage, USA

Ro. J. Techn. Sci. − Appl. Mechanics, Vol. 69, N° 1, P. 3–33, Bucharest, 2024

DOI:10.59277/RJTS-AM.2024.1.01

of such a hinge are to be minimized since they generate “parasitic” (unwanted) motions. The design of Fig. 1a, which is one-dimensional (1D) because of its straight-line longitudinal axis, can be very stiff in all deformation directions except the bending axis. At the other end of the spectrum, the hinge of Fig. 1b is defined by a spatial axial curve and is therefore three-dimensional (3D). This design combines bending with torsion and axial deformations resulting in a more complex motional output, and is therefore more appropriately called flexible hinge. Moreover, the hinge of Fig. 1b is constructed by serially linking several (multiple) flexible segments, which makes the design low-stiffness (soft).

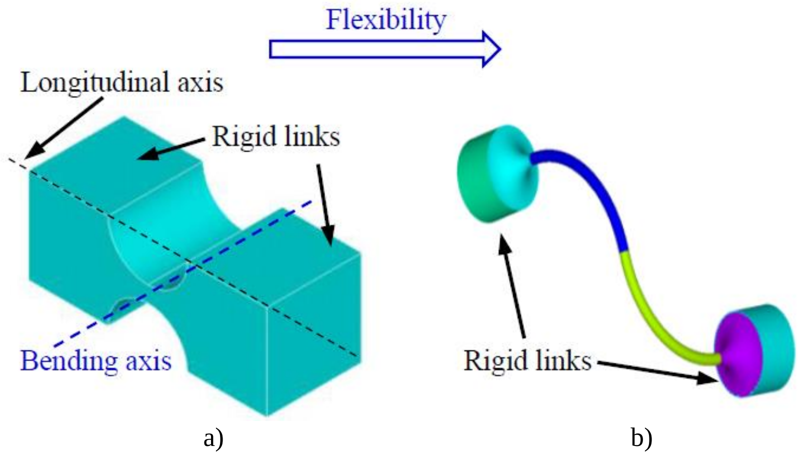


Fig. 1 – Two flexible hinges: a) 1D, single-segment, circular design;
b) 3D, multiple serially-connected segments.

1D straight-axis flexure hinges may be designed by using a segment whose longitudinal profile is defined by a single curve or by linking in series multiple segments of different longitudinal profiles. Several 1D hinge configurations have been studied in terms of their compliance or stiffness, including longitudinal profiles such as circular, elliptical, corner-filleted, conic-section, V-shaped, polynomial-curve, power-function, Bézier-curve or NURBS – [1–16]. The straight-axis flexure hinges quasi-static behavior has mainly been characterized by means of analytical and numerical methods, including the analytical compliance/stiffness matrix approach and the finite element technique – [4], the extended compliance matrix procedure – [5] and the discrete-beam transfer matrix method – [6]. Expanding the deformation capabilities of straight-axis, 1D hinge configurations are the two-dimensional (2D) flexible hinges, which either are made of a single segment or combine segments with planar-curve longitudinal axes that may include straight-axis segments, as studied in [4] and [17–24], for instance. Further enhancing the motion spectrum necessary in mechanisms for precision positioning and manipulation are the serial flexible hinges of 3D configuration, such as those presented in [25, 26] – Fig. 1b depicts such a 3D hinge design. Cross-axis flexure hinges, described in [27–29] for instance, and lattice-type flexures, such as those presented in [30, 31] are also monolithic hinges of 3D structure with parallel-connection members.

As already mentioned, the deformation capabilities of monolithic hinges range from very stiff to very flexible depending on the shape of the cross-section, the longitudinal profile of the segment curves that form the hinge, and the geometric dimensions. Highly flexible hinges can be designed based on a large overall length, which can be generated within a reasonable geometrical envelope by folding the segments in a dense manner, as exemplified by the 2D serpentine configurations of [4, 32–35] and the 2D designs of [36, 37] among others.

The hinge design proposed here is a 3D configuration that uses the principle of serially folding multiple segments, of either circular or straight axis, in a spatial architecture in order to generate large displacements in applications requiring coverage of an extended 3D workspace. A simpler, but similar, 3D folded hinge design was recently introduced and studied – [38]. The hinge of this paper can be incorporated in flexible positioning/manipulating mechanisms, soft robotic arms, dexterous compliant grippers, wearable haptic devices, flexible electronics, tunable stiffness mechanisms, prosthetics, joy-stick mechanisms, elastic suspensions, monolithic bearings, 3D stages, bi-stable devices, precision tracking devices, laser optics flexible fixtures, gyroscopes, 3D displacement compliant sensors (seismometers), and sensing/actuation systems where control and linear behavior over a wide displacement range are necessary.

We derive an accurate linear analytical compliance model, which also includes the allowable material stress to predict the maximum applicable loads and related displacements generated by this hinge. The compliance matrix model has successfully been utilized in several other flexible-hinge applications – see [4, 25, 26] for instance. The model developed here employs closed-form compliances of straight- and circular-axis segments and combines them into the global-frame 3D compliance matrix of the hinge. One key advantage of this model, which is based on the compliance/flexibility concept introduced in the 1950s (see [1]) in the context of compliant mechanisms, is that it needs one element only (and one compliance matrix) for each straight- and circular-axis segment of the hinge.

A list of benefits/advantages of the proposed 3D serial-connection flexible hinge, as compared to 1D, 2D or other existing 3D hinge designs, includes the following:

- structure with multiple serially-connected flexible segments, which enables the adjacent rigid links to undergo large motions and cover an extended 3D space;
- multiple geometric parameters, which provide more options in adjusting the hinge deformation capability and motional pattern;
- folded design, which maintains a relatively small 3D envelope of the hinge;

- enhanced capacity of translation and/or rotation in 3D, which enables the hinge moving end to perform complex spatial motions;
- improved coupling between the 6 degrees of freedom of the hinge mobile end due to the particular design of the hinge and the resulting compliance matrix; the motion coupling contributes to increasing the versatility of the overall hinge motion;
- relatively simple design, which facilitates fabrication and implementation in actual applications;
- modular design based on quarter portions arranged in parallel layers; the specific design presented here can easily be extended by increasing the number of circular-axis segments in a quarter, as well as by increasing the number of parallel layers; these structural alterations can modify substantially the hinge response while preserving the structure of the compliance-based analytical model;
- simple linear-domain analytical model that requires one compliance matrix for each component; the matrix uses closed-form compliances that are available for the hinge straight- and circular-axis segments;
- the hinge is capable of maintaining the load-displacement linearity over a larger domain, which makes it appealing to sensing/actuation control applications;
- because all deformations produced through bending, torsion and axial loads are enabled, there are no marked “parasitic” motions to limit the 3D reach of the hinge;

Compared to the 3D hinge configurations described in [25, 26, 38], the hinge proposed here is capable of generating larger displacements while accommodating higher loads in the linear domain given its multiple serially-connected flexible segments. As a result, the moving end of this hinge can cover a wider 3D space. Owing to the same structure, this design is more sensitive to external loading action and is therefore applicable in sensing/actuation systems where increased accuracy and precision are required. As mentioned previously, despite being constructed from multiple components, the four-quarter, two-plane, folded configuration results in a compact, relatively small-footprint hinge design. The analytical compliance matrix model is reduced as it employs a simplified hinge geometry that eliminates the small filleted regions. The analytical model is utilized to perform a comprehensive parametric study of the hinge elastic response with respect to scaling (individual and overall), particular motions (the piston-type translation), and stress-based maximum loads/displacements.

The paper is structured in two main sections. In the first part, which is focused on analytical modelling, the compliance matrix of the new flexible hinge is formulated by utilizing a simplified geometry. The model validity is verified by both finite element simulation and experimental testing of a fabricated specimen. The analytical compliance matrix is also utilized to characterize the hinge piston-motion stiffness, as well to predict the displacements resulting from the maximum load permitted by the allowable equivalent stress in the hinge. The second part of the paper employs the mathematical models to perform a comprehensive study of the effect of geometric parameters variation on compliances, as well as on the stress-related maximum load and displacements.

## 2. NEW 3D SERIAL FLEXIBLE HINGE

Figure 2 is a drawing of the proposed 3D flexible hinge. The hinge serially links several straight-axis segments and circular-axis segments starting from *O* and ending at *A*. Figure 2 also shows the six loads (three forces and thee moments) that are applied at the hinge moving end *O* in the Cartesian reference frame *Oxyz*.

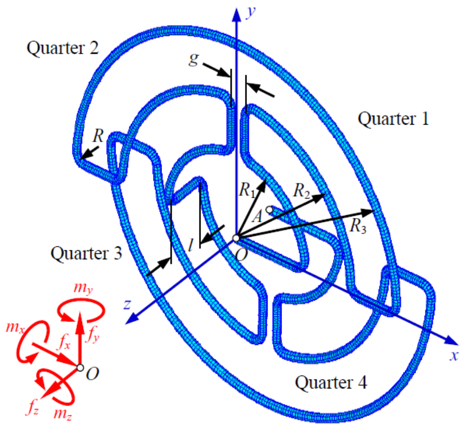


Fig. 2 – New 3D flexible hinge configuration.

Structurally, the hinge is formed of two identical halves that are mirrored with respect to the *xz* plane of the reference system *Oxyz*; the two halves are offset a distance *l* along the *z* axis. The half that is placed in the *xy* plane can further be divided into two quarter portions (quarter 1 is in the plane of the positive *x*, *y* axes and quarter 2 is in a plane defined by the negative *x* axis and the positive *y* axis). The other half of the hinge can similarly be split into two other quarter regions: quarter 3, which is identical to quarter 1, and quarter 4, which is identical to quarter 2. Section 3 offers more geometric details, but, as shown in Fig. 2, each quarter includes three concentric circular sectors of medium radii $R_1$, $R_2$, $R_3$ and two or three shorter, straight-axis segments. To reduce stress concentration at the junctions between adjacent segments, short, circular-axis fillets of medium radius *R* are employed. The hinge has all segments designed with the same constant circular cross-section of diameter *d*, but other cross-section shapes (such as rectangular or square) can be utilized.

Due to its large number of serially-connected segments, this particular hinge configuration is aimed at realizing high levels of flexibility with respect to the six degrees of freedom of the moving end, which facilitates its incorporation in compliant devices with end effectors required to cover a wide workspace, such as in robotic manipulation. At the same time, the hinge folded architecture results in a densely-packed, compact design, which reduces the overall geometric footprint. The hinge structure is modular and relatively simple (at it consists of straight- and circular-axis segments only); this feature, on one hand, facilitates the derivation of closed-form, accurate analytical models (as detailed in section 3) and, on the other hand, enables scaling up this particular configuration to designs that have more than three concentric circular segments and more than two layers (planes), for instance.

## 3. ANALYTICAL COMPLIANCE MATRIX MODELS

The first part of this section derives the analytical compliance matrix, which connects the end load vector to the resulting displacement vector for the new 3D flexible hinge. The second part of the section evaluates the maximum load that can safely be applied to the hinge and the resulting hinge deformations/displacements by considering the allowable stress levels and the compliance matrix.

### 3.1. Compliance matrix

Using a matrix approach, the flexible hinge compliance matrix is derived here by using a simplified geometry. The compliance matrix is also utilized to evaluate the hinge piston-motion stiffness, as well as the elastic response of several identical and serially-connected flexible hinges. The analytical model predictions are validated both by finite element analysis and experimentally through testing of a hinge prototype. The finite element simulation also identifies a criterion for establishing the accuracy and validity limits of the simplified-geometry analytical model.

#### 3.1.1. Model derivation

The simplified, skeleton-form design of Fig. 3a only retains the straight- and circular-axis segments by removing the small filleted portions shown in Fig. 2 and Fig. 3b. This simplified geometry serves at deriving the compliance matrix $\boldsymbol{C}_O$ that relates the 3D load vector $\boldsymbol{f} = [f_x \;\; f_y \;\; m_z \;\; m_x \;\; m_y \;\; f_z]^{\mathrm{T}}$ applied at the moving end $O$ of the flexible hinge to the resulting displacement vector $\boldsymbol{u} = [u_x \;\; u_y \;\; \theta_z \;\; \theta_x \;\; \theta_y \;\; u_z]^{\mathrm{T}}$ at the same point when the other end $A$ is fixed (see Fig. 2). The symbols $f$, $m$, $u$ and $\theta$ denote force, moment, displacement and rotation angle, respectively. The two vectors are connected by the compliance matrix in the form: $\boldsymbol{u} = \boldsymbol{C}_O \boldsymbol{f}$. The design of Fig. 3b, which depicts the same hinge with filleted junction portions, will be utilized for finite element simulation, as well as for the fabricated specimen used in experimental testing later in this section.

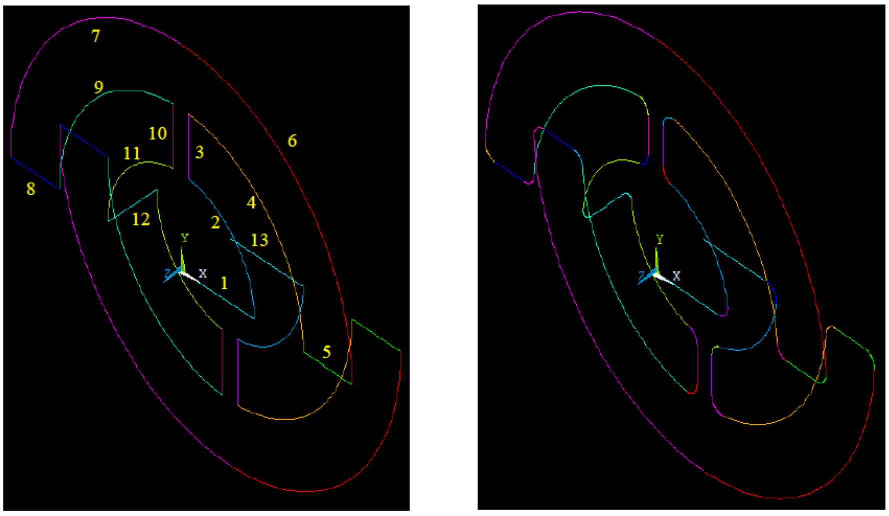


a) b)

Skeleton configurations of new 3D hinge: a) simplified with sharp vertices; b) actual with rounded (filleted) vertices.

The 6 × 6 symmetric matrix $\boldsymbol{C}_O$ is formed of elements $C_{ij}$ ($i$, $j$ = 1 to 6 and $C_{ij} = C_{ji}$). To conform with the sequence of both $\boldsymbol{u}$ and $\boldsymbol{f}$, the compliance numerical subscripts $i$, $j$ have the following meaning: 1 is used for $x$-axis translation, 2 for $y$-axis translation, 3 for $z$-axis rotation, 4 for $x$-axis rotation, 5 for $y$-axis rotation, and 6 for $z$-axis translation. The first subscript denotes a displacement while the second subscript identifies a load; for instance, $C_{ij}$ refers to the compliance expressing the displacement $i$ that is produced by the load $j$.

To calculate $\boldsymbol{C}_O$, the hinge is partitioned in four structurally-identical quarters, which are depicted in Figs. 4 a, b, d and e, and three straight-axis segments shown in Figs. 4c, f and g. Each segment is identified by its local reference frame in Figs. 4a, b, c, f, g. Quarter 1 of Fig. 4b is formed of segments 2 through 6, quarter 2 of Fig. 4a comprises segments 7 through 11, while quarters 3 and 4 (sketched in Figs. 4d and e) have compliance properties that result from those of quarters 1 and 2, as demonstrated shortly. Segment 1 of Fig. 4c, together with segment 12, which connects the two planes of the hinge and is depicted in Fig. 4f, as well as the last segment 13, complete the hinge structure. The 13 segments are also indicated by numbers in Fig. 3a. These segments, as well as quarters 3 and 4, are accompanied by their local frames in Fig. 4.

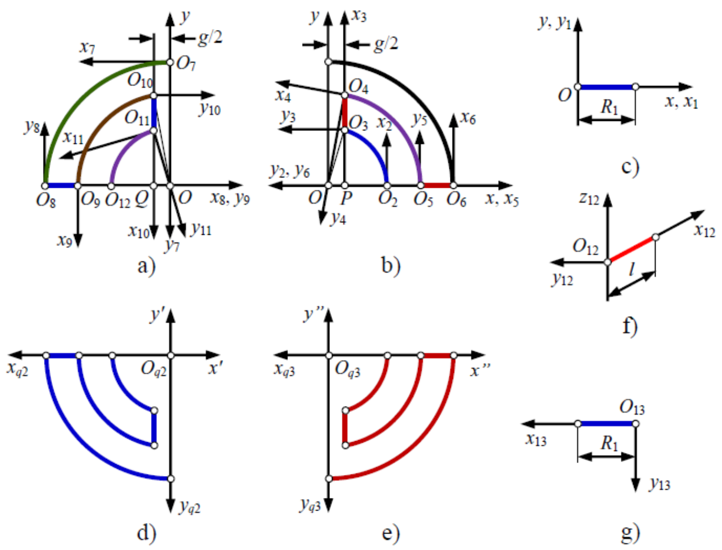

Fig. 4 – Geometry and local reference frames of: a) quarter 2; b) quarter 1; c) segment 1; d) quarter 3; e) quarter 4; f) segment 12; g) segment 13.

Because all these segments are connected in series, the hinge compliance matrix is calculated with respect to the global frame *Oxyz* located at end *O* by summing the compliance matrices of the components just described, namely:

$$\boldsymbol{C}_O = \boldsymbol{C}_O^{(1)} + \boldsymbol{C}_O^{(q_1)} + \boldsymbol{C}_O^{(q_2)} + \boldsymbol{C}_O^{(12)} + \boldsymbol{C}_O^{(q_3)} + \boldsymbol{C}_O^{(q_4)} + \boldsymbol{C}_O^{(13)}, \tag{1}$$

where the superscript $q_i$ refers to the quarter $i$ ($i$ = 1, 2, 3, 4). The compliance matrices of quarters 1 and 2 are similarly determined by adding the compliance matrices of their segments, namely:

$$\begin{aligned}
\boldsymbol{C}_O^{(q_1)} &= \sum_{i=2}^{6} \boldsymbol{C}_O^{(i)} = \sum_{i=2}^{6} \boldsymbol{T}_{OO_i}^{(i)\,T} \boldsymbol{R}^{(i)T} \boldsymbol{C}_{O_i}^{(i)} \boldsymbol{R}^{(i)} \boldsymbol{T}_{OO_i}^{(i)}, \\
\boldsymbol{C}_O^{(q_2)} &= \sum_{i=7}^{11} \boldsymbol{C}_O^{(i)} = \sum_{i=7}^{11} \boldsymbol{T}_{OO_i}^{(i)\,T} \boldsymbol{R}^{(i)T} \boldsymbol{C}_{O_i}^{(i)} \boldsymbol{R}^{(i)} \boldsymbol{T}_{OO_i}^{(i)}, \\
\boldsymbol{C}_O^{(i)} &= \boldsymbol{T}_{OO_i}^{(i)\,T} \boldsymbol{R}^{(i)T} \boldsymbol{C}_{O_i}^{(i)} \boldsymbol{R}^{(i)} \boldsymbol{T}_{OO_i}^{(i)}, \; i = 12{,}13.
\end{aligned} \tag{2}$$

Equation (2) transforms the local-frame compliance matrices $\boldsymbol{C}_{O_i}^{(i)}$ of the segments identified in the summation symbols into the corresponding global-frame compliance matrices $\boldsymbol{C}_O^{(i)}$ by means of translation matrices $\boldsymbol{T}_{OO_i}^{(i)}$ and rotation matrices $\boldsymbol{R}^{(i)}$. The same Eq. (2) also includes the compliance matrices of elements 12 and 13 with respect to the global frame. For segment 1, whose local frame coincides with the global frame, the global-frame and local-frame compliance matrices are identical, which is: $\boldsymbol{C}_O^{(1)} = \boldsymbol{C}_{O_1}^{(1)}$. Since all component (individual) segments are planar, their 6 x 6 local-frame compliance matrices can be partitioned as:

$$\boldsymbol{C}_{O_i}^{(i)} = \begin{bmatrix} \boldsymbol{C}_{O_i,ip}^{(i)} & \mathbf{0} \\ \mathbf{0} & \boldsymbol{C}_{O_i,op}^{(i)} \end{bmatrix}. \tag{3}$$

The subscript "*ip*" in Eq. (3) denotes in-plane elements while "*op*" in the same equation represents out-of-plane elements. The in-plane degrees of freedom are $u_x$, $u_y$ and $\theta_z$ whereas the out-of-plane degrees of freedom are $\theta_x$ , $\theta_y$ and $u_z$. Consequently, and consistent with the structure of $\boldsymbol{u}$ and $\boldsymbol{f}$, the in-plane compliance submatrices of Eq. (3) are formulated as:

$$\begin{aligned} &\text{Straight axis: } \boldsymbol{C}_{O_i,ip}^{(i)} = \begin{bmatrix} C_{11}^{(i)} & 0 & 0 \\ 0 & C_{22}^{(i)} & C_{23}^{(i)} \\ 0 & C_{23}^{(i)} & C_{33}^{(i)} \end{bmatrix}; \\ &\text{Circular axis: } \boldsymbol{C}_{O_i,ip}^{(i)} = \begin{bmatrix} C_{11}^{(i)} & C_{12}^{(i)} & C_{13}^{(i)} \\ C_{12}^{(i)} & C_{22}^{(i)} & C_{23}^{(i)} \\ C_{13}^{(i)} & C_{23}^{(i)} & C_{33}^{(i)} \end{bmatrix}. \end{aligned} \tag{4}$$

The out-of-plane compliance submatrices matrix of Eq. (3) are expressed as:

$$\begin{aligned} &\text{Straight axis: } \boldsymbol{C}_{O_i,op}^{(i)} = \begin{bmatrix} C_{44}^{(i)} & 0 & 0 \\ 0 & C_{33}^{(i)} & -C_{23}^{(i)} \\ 0 & -C_{23}^{(i)} & C_{22}^{(i)} \end{bmatrix}; \\ &\text{Circular axis: } \boldsymbol{C}_{O_i,op}^{(i)} = \begin{bmatrix} C_{44}^{(i)} & C_{45}^{(i)} & C_{46}^{(i)} \\ C_{45}^{(i)} & C_{55}^{(i)} & C_{56}^{(i)} \\ C_{46}^{(i)} & C_{56}^{(i)} & C_{66}^{(i)} \end{bmatrix}. \end{aligned} \tag{5}$$

The local-frame compliances of straight- and circular-axis segments are provided in [4]. While the rotations of segments 1 through 11 are planar, the rotation of segment 12, as seen in Fig. 4f, is spatial. *Appendix A* includes the equations of translation and rotation matrices equations together with the rotation angles and local-frame offsets of segments 2 through 13.

Comparing Figs. 4b and d with Fig. 3a, it can be seen that quadrant 3 results from a π (180°) *z*-axis rotation of quadrant 1; similarly, quadrant 4 is quadrant 2 rotated around the *z* axis by π – see Figs. 4a, 4e and 3a. As a consequence, the global-frame compliance matrices of quadrants 3 and 4 are calculated as:

$$\boldsymbol{C}_O^{(q_3)} = \boldsymbol{R}^{(q_3)T}\boldsymbol{C}_O^{(q_1)}\boldsymbol{R}^{(q_3)}; \quad \boldsymbol{C}_O^{(q_4)} = \boldsymbol{R}^{(q_3)T}\boldsymbol{C}_O^{(q_2)}\boldsymbol{R}^{(q_3)}. \tag{6}$$

The rotation matrix of Eq. (6) is calculated as in *Appendix B* by using the angles $\varphi = \pi$, $\theta = 0$, $\psi = 0$. The circular-axis segments 4 and 10 of Figs. 4a and b have their local axes rotated (flipped) around the $y_i$ axes. This flip/mirroring results in minus signs in front of the cross compliances $C_{12}^{(i)}$, $C_{23}^{(i)}$, $C_{45}^{(i)}$, $C_{56}^{(i)}$ in Eqs. (4) and (5) – more details about flipping/mirroring are provided in [4].

Closed-form expressions of the 21 components of the compliance matrix $\boldsymbol{C}_O$ are obtained based on Eqs. (1) through (6) in conjunction with the equations and tables of *Appendix A*; these algebraic expressions are quite complex and are not provided here.

In addition to fully characterizing the direct/inverse kinematics of the hinge, the compliance matrix $\boldsymbol{C}_O$ can be employed to calculate the piston-motion stiffness when the flexible hinge undergoes translation along the $z$ axis under the action of a force along the same axis, as well as the compliance matrix of a design that links several hinges in series; those two design models are discussed next.

a) *Constrained z-axis translation (piston motion)*. One particular motion of the flexible hinge is the piston motion, or translation along the $z$ axis. In this case, a force $f_z$ applied at the moving end $O$ of the hinge generates a displacement $u_z$ at the same point, as sketched in Fig. 5a.

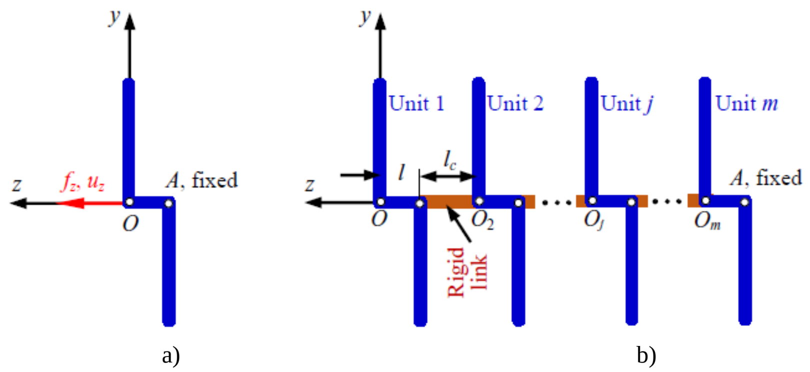


Fig. 5 – Side views of hinges with end constrained to $z$-axis translation: a) one flexible hinge; b) $m$ identical flexible-hinge units connected in series.

In order for this motion to occur, the translations and rotations along the $x$ and $y$ axes (perpendicular to the motion direction $z$) are prevented at $O$, which means: $u_x = 0$, $u_y = 0$, $\theta_x = 0$ and $\theta_y = 0$. Corresponding to these boundary conditions, the reactions $R_x$, $R_y$, $M_x$ and $M_y$ are applied to the hinge at $O$ by the external support blocking the above-mentioned degrees of freedom. As a consequence, the following explicit equation results from the general equation $\boldsymbol{u} = \boldsymbol{C}_O\,\boldsymbol{f}$:

$$\begin{bmatrix} R_x \\ R_y \\ M_x \\ M_y \end{bmatrix} = \begin{bmatrix} C_{11} & C_{12} & C_{14} & C_{15} \\ C_{12} & C_{22} & C_{24} & C_{25} \\ C_{14} & C_{24} & C_{44} & C_{45} \\ C_{15} & C_{25} & C_{45} & C_{55} \end{bmatrix}^{-1} \begin{bmatrix} -C_{16} \\ -C_{26} \\ -C_{46} \\ -C_{56} \end{bmatrix} f_z, \tag{7}$$

where $\boldsymbol{u} = [0\ \ 0\ \ \theta_z\ \ 0\ \ 0\ u_z]^{\mathrm{T}}$, $\boldsymbol{f} = [R_x\ \ R_y\ \ 0\ \ M_x\ \ M_y\ \ f_z]^{\mathrm{T}}$, and the compliances are elements of the 6 x 6 hinge compliance matrix $\boldsymbol{C}_O$. Eq. (7) is solved for the reaction forces/moments, which are of the form:

$$R_x = c_1 f_z,\ R_y = c_2 f_z,\ M_x = c_3 f_z,\ M_y = c_4 f_z\ , \tag{8}$$

where $c_i$ ($i$ = 1, 2, 3, 4) are constant factors depending on compliances. The reactions of Eq. (8) are substituted in the last individual algebraic equation of $\boldsymbol{u} = \boldsymbol{C}_O\ \boldsymbol{f}$, which yields the hinge stiffness corresponding to the $z$-axis translation:

$$k_z = \frac{f_z}{u_z} = \frac{1}{c_1 C_{16} + c_2 C_{26} + c_3 C_{46} + c_4 C_{56} + C_{66}}. \tag{9}$$

It should be noted that with the set boundary conditions, the free end of the hinge is allowed to have a $\theta_z$ rotation, which can be evaluated using the particular equation expressing $\theta_z$ (from the vector equation $\boldsymbol{u} = \boldsymbol{C}_O \boldsymbol{f}$) once the reactions of Eq. (8) have been found. The nonzero displacement $u_z$ and rotation $\theta_z$ that result from the specified boundary conditions describe a twist screw motion. However, the nonzero rotation angle $\theta_z$ does not affect the correctness of the translation stiffness formulated in Eq. (9).

b) *Series connection of several flexible hinges*. To further increase the displacement of a single flexible hinge, several hinge units can be connected in series, as depicted in the schematic representation of Fig. 5b, which shows a train of $m$ identical hinges coupled in series by means of identical and rigid links of length $l_c$. The compliance matrix $\boldsymbol{C}_{O,m}$ of this generic design is calculated as:

$$\boldsymbol{C}_{O,m} = \boldsymbol{C}_O + \sum_{j=1}^{m-1} \boldsymbol{T}_{OO_j}^{(j)\,T} \boldsymbol{C}_O \boldsymbol{T}_{OO_j}^{(j)}, \tag{10}$$

where $\boldsymbol{C}_O$ is the local-frame compliance matrix of one flexible hinge unit – see Eq. (1). Equation (10) points out that the $m$ – 1 hinge units that are translated from the global origin $O$ need to be transformed by means of translation matrices (calculated as in *Appendix A*), whose offsets are: $\Delta x_j = 0$, $\Delta y_j = 0$, $\Delta z_j = -(j-1)(l_c + l)$, where $j$ = 1, 2, …, $m$ and $l_c$ is the $z$-axis offset between two adjacent units – see Fig. 5b.

### 3.1.2. Model validation

The accuracy of the analytical compliance model of section 3.1.1 was verified by means of finite element performed with ANSYS, as well as by experimental testing of a prototype. Both methods generated results that were very close to the analytical model predictions, which confirmed the validity of the analytical model.

a) *Finite element simulation*. The analytical compliances were compared to the compliances resulting from finite element (FE) simulation performed in ANSYS by using several hinge designs of which Table 1 lists five configurations with their geometric parameters. The finite element model utilized the hinge geometry with filleted corners that is depicted in Fig. 2 and Fig. 3b. The finite element model was built with 3D beam elements having two end nodes and 12 degrees-of-freedom (DOF) – six DOF at each node. Several meshing densities were tested in order to identify a variant that generates results of sufficient accuracy with a relatively small number of elements. The selected mesh was formed of 10 elements for both the circular filleted portions and all the straight-axis segments, 20 elements for the circular segments of radius $R_1$, 50 elements for the circular segments of radius $R_2$, and 80 elements for the circular segments of radius $R_3$. The material properties used by both the analytical and finite element simulation were: Young's modulus $E = 1.2 \cdot 10^{11}$ N/m$^2$ and Poisson's ratio $\mu = 0.3$.

*Table 1*

Hinge designs with geometric parameter dimensions (in [mm])

| Design | $d$ | $R_1$ | $R_2$ | $R_3$ | $R$ | $l$ | $g$ |
|---|---|---|---|---|---|---|---|
| 1 | 2 | 10 | 20 | 30 | 1.5 | 6 | 2$d$ |
| 2 | 2.5 | 10 | 20 | 30 | 2 | 6 | 1.5$d$ |
| 3 | 3 | 10 | 25 | 40 | 1.8 | 10 | 1.5$d$ |
| 4 | 3.5 | 15 | 30 | 40 | 1 | 12 | 1.5$d$ |
| 5 | 3.5 | 15 | 30 | 40 | 3.75 | 12 | 1.5$d$ |

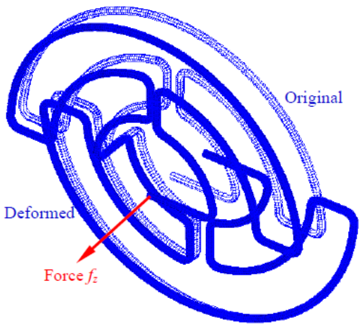


Fig. 6 – Finite element model of flexible hinge with axial force $f_z$.

Figure 6 shows the hinge finite-element deformed shape after applying a force $f_z$ at one end while the other end is fixed. The 21 finite element compliances were obtained in ANSYS by means of the following procedure. A force $f_x = 1$ N was applied at the hinge moving end and a static analysis was performed. The resulting 3 displacements and 3 rotations at the same point are the 6 compliances in the first row of $\boldsymbol{C}_O$. The force $f_x$ was then deleted and a force $f_y = 1$ N was applied at the same point, which provided the 6 compliances in the second row of $\boldsymbol{C}_O$ after running another static analysis. This sequence continued for the remaining four load components of $\boldsymbol{f}$, which produced the elements in the last four rows of $\boldsymbol{C}_O$.

Table 2 lists 5 of the 21 compliances that form the matrix $\boldsymbol{C}_O$. As the table results show, the deviations of the analytical model predictions from the finite element model results are all less than 4% for the first four designs; similar results and relative differences were noted for the other compliances not listed in Table 2.

*Table 2*

Analytical-model (*A*), finite-element model (*FE*) compliances and relative differences (*rd*)

| Design | Results | $C_{u_x-f_x}$ [$N^{-1}m$] | $C_{u_y-f_y}$ [$N^{-1}m$] | $C_{u_y-m_x}$ [$N^{-1}$] | $C_{\theta_z-m_z}$ [$N^{-1}m^{-1}$] | $C_{u_z-f_z}$ [$N^{-1}m$] |
|---|---|---|---|---|---|---|
| 1 | *A* | $1.36\cdot10^{-4}$ | $1.59\cdot10^{-3}$ | $-1.71\cdot10^{-2}$ | 4.98 | $3.45\cdot10^{-3}$ |
| | *FE* | $1.34\cdot10^{-4}$ | $1.55\cdot10^{-3}$ | $-1.67\cdot10^{-2}$ | 4.85 | $3.39\cdot10^{-3}$ |
| | *rd* [%] | 1.47 | 2.52 | 2.34 | 2.61 | 1.74 |
| 2 | *A* | $5.59\cdot10^{-4}$ | $6.52\cdot10^{-4}$ | $-7.02\cdot10^{-3}$ | 2.04 | $1.41\cdot10^{-3}$ |
| | *FE* | $5.47\cdot10^{-4}$ | $6.28\cdot10^{-4}$ | $-6.77\cdot10^{-3}$ | 1.97 | $1.38\cdot10^{-3}$ |
| | *rd* [%] | 2.15 | 3.68 | 3.56 | 3.43 | 2.13 |
| 3 | *A* | $6.35\cdot10^{-4}$ | $7.44\cdot10^{-4}$ | $-7.26\cdot10^{-3}$ | 1.27 | $1.51\cdot10^{-3}$ |
| | *FE* | $6.22\cdot10^{-4}$ | $7.27\cdot10^{-4}$ | $-7.09\cdot10^{-3}$ | 1.24 | $1.52\cdot10^{-3}$ |
| | *rd* [%] | 2.05 | 2.28 | 2.34 | 2.36 | 0.66 |
| 4 | *A* | $4.19\cdot10^{-4}$ | $4.6\cdot10^{-4}$ | $-5.09\cdot10^{-3}$ | 0.746 | $9.53\cdot10^{-4}$ |
| | *FE* | $4.16\cdot10^{-4}$ | $4.54\cdot10^{-4}$ | $-5.04\cdot10^{-3}$ | 0.737 | $9.44\cdot10^{-4}$ |
| | *rd* [%] | 0.72 | 1.3 | 0.98 | 1.21 | 0.94 |
| 5 | *A* | $4.19\cdot10^{-4}$ | $4.6\cdot10^{-4}$ | $-5.09\cdot10^{-3}$ | 0.746 | $9.53\cdot10^{-4}$ |
| | *FE* | $4.07\cdot10^{-4}$ | $4.4\cdot10^{-4}$ | $-4.9\cdot10^{-3}$ | 0.708 | $9.18\cdot10^{-4}$ |
| | *rd* [%] | 2.86 | 4.35 | 3.73 | 5.09 | 3.67 |

The small differences between the two models indicate that the simplified-geometry analytical model generates accurate results and, therefore, this model can confidently be utilized for design/analysis purposes.

It should be reminded that the actual geometry of the hinge – see Fig. 3b – adds the fillet regions to the simplified configuration of Fig. 3a. However, the fillet radius is relatively small, since it is only employed to eliminate sharp corners and diminish the related stress concentration effects. Consequently, the relatively-short filleted segments should not substantially affect either the overall elasticity of the hinge or the analytical model accuracy that is based on the fillet-less, simplified geometry. The filet radius value effect on compliances can be seen in Table 2 where the relative errors between analytical and finite element results are a bit higher for larger fillet radii, such as the case is with Design 2 where $R$ = 2 mm. Several other designs, whose results are not included here, were also tested by comparing the compliances of the simplified-geometry analytical model to those of the finite element model with filleted corners in order to identify some threshold metric of the analytical model validity. The results indicated that a critical parameter that should be used in evaluating the validity of the simplified analytical model is the ratio $R_1/R$; specifically, it was observed that the errors of the analytical model results are larger than 5% for ratio $R_1/R$ values approximately smaller than 4. This is illustrated by the last configuration, Design 5 where $R_1/R$ = 4; the fillet radius value is the only geometric difference between Designs 4 and 5.

b) *Experimental testing*. Figure 7a is the photograph of a flexible hinge prototype that was designed and fabricated from plastic material (PolyJet$^{TM}$ Material Simulating Engineering Plastics) using a 3D printer (Object260 Connex3) and typical fused deposition. The prototype's dimensions, which are graphically defined in Fig. 2, were: $d$ = 4.762 mm, $R_1$ = 25.4 mm, $R_2$ = 38.1 mm, $R_3$ = 50.8 mm, $l$ = 6.35 mm, $g$ = 9.525 mm and $R$ = 2.54 mm.

a)

b)

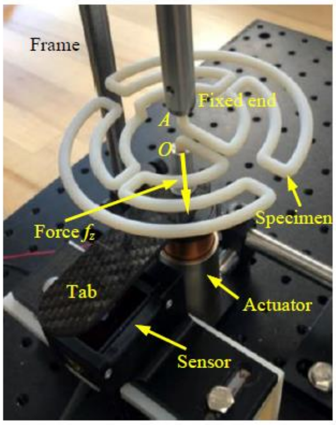


Fig. 7 – Photographs of: a) 3D printed hinge specimen; b) experimental setup.

The experimental setup that was utilized to test the specimen is shown in the photograph of Fig. 7b. A vertical, adjustable frame was connected to a fixed optical board. The 3D flexible hinge was attached at one end to the frame, which enabled to adjust the hinge position in two directions along the $x$ and $z$ axes (see also Fig. 2). A voice-coil (translation) actuator attached at the other end of the hinge forced the specimen into a $z$-axis translation at that end. The deformation motion of the hinge mobile end was monitored by a laser displacement sensor that was affixed to the optical board through an additional part enabling the sensor vertical position to be adjusted within operational range. The incoming rays of the sensor were reflected back by a carbon-fiber tab, which was attached to the actuator. Three separate experimental test runs were performed, each consisting of 10–12 measuring points that covered the linear force-displacement domain. The linearity and consistency of these results were very good and they resulted in the following values of the $z$-axis experimental stiffness $k_z = f_z/u_z$: 37 N/m (twice) and 36 N/m. All three experimental test sets revealed the remarkable linear force-displacement hinge characteristic for maximum displacements $u_z$ of more than 0.025 m.

The analytical model was also utilized to obtain the $z$-axis stiffness and compare it to the experimental stiffness results. Given the piston motion generated by the actuator, the stiffness $k_z$ was calculated by means of Eqs. (1) through (9). With the plastic-material Young's modulus $E = 2.61 \cdot 10^9$ N/m$^2$ and Poisson's ratio $\mu = 0.35$, the analytical value of the stiffness was $k_z = f_z/u_z = 36.031$ N/m, which is an excellent match of the experimental stiffness. It should be pointed out that compared to the analytical and finite element geometric models, the fabricated prototype has two extra straight-axis segments at its ends, which were needed to place and secure the specimen in its test setup. However, these two segments were very short and did not influence the analytical model predictions, as illustrated by the analytical versus experimental stiffness values.

Section 4 comprises a part that studies the quantitative dependence of the individual compliances of $\boldsymbol{C}_O$ on the geometric parameters defining the new 3D hinge by using the simplified-geometry analytical model of this section.

### 3.2. Stress-based maximum loads and displacements

The load vector $\boldsymbol{f}$ that can safely be applied at one end of the hinge is limited by and can be assessed in terms of the maximum stress levels. With the safe load, the maximum displacement vector $\boldsymbol{u}$ is determined by means of the hinge compliance matrix as $\boldsymbol{u} = \boldsymbol{C}_O \boldsymbol{f}$. Under load, the flexure hinge cross-section is subjected mainly to bending around two perpendicular directions, axial load and torsion. As a result, normal stresses $\sigma$ and tangential stresses $\tau$ are produced in the hinge cross-section, which can be combined into an equivalent normal stress $\sigma_{eq}$ by means of available yield criteria, such as the von Mises criterion, according to which:

$$\sigma_{eq} = \sqrt{\sigma^2 + 3\tau^2}\ . \qquad (11)$$

Equation (11) may also be utilized at limit when the equivalent stress becomes the material allowable stress $\sigma_a$ while the normal and tangential stresses are maximum: $\sigma_{\max}$, $\tau_{\max}$. Due to the load being applied at the free end *O*, the maximum load of the flexible hinge is at the fixed end *A* where the stresses are also maximum. The normal stress, which occurs at a point on the cross-section circumference, is generated by the bending moment $M_b$ and normal force *N*, and is calculated as:

$$\begin{aligned}\sigma_{\max} &= \frac{M_b d}{2I} + \frac{N}{A} = \frac{d\sqrt{M_y^2 + M_z^2}}{2I} + \frac{N}{A} = \\ &= \left(\frac{32}{\pi d^3}\right)\sqrt{M_y^2 + M_z^2} + \left(\frac{4}{\pi d^2}\right)N,\end{aligned} \tag{12}$$

where $A = \pi d^2/4$ and $I = \pi d^4/64$ are the circular cross-section area and area moment of inertia with respect to a central axis. Eq. (12) took into account that $M_b = \sqrt{M_y^2 + M_z^2}$ . The maximum tangential stress, which is due to the torsion moment $M_t$, occurs on the circumference, as well, and has the following equation:

$$\tau_{\max} = \frac{M_t d}{2I_p} = \left(\frac{16}{\pi d^3}\right)M_t, \tag{13}$$

where $I_p = \pi d^4/32$ is the circular cross-section polar moment of inertia.

To evaluate $M_y$, $M_z$, *N* and $M_t$ at the root *A*, the load vector $\boldsymbol{f}$ applied at *O* is translated at *A* based on the transformation equation:

$$\begin{aligned}\boldsymbol{f}_A = \boldsymbol{T}_{OA}\boldsymbol{f} \quad \text{or} \quad &\begin{bmatrix} f_{Ax} & f_{Ay} & m_{Az} & m_{Ax} & m_{Ay} & f_{Az}\end{bmatrix}^T = \\ &= [\boldsymbol{T}_{OA}]\begin{bmatrix} f_x & f_y & m_z & m_x & m_y & f_z\end{bmatrix}^T.\end{aligned} \tag{14}$$

The translation matrix of Eq. (14) is calculated as in *Appendix A* with the following offsets (measured from *O* to *A* in the global frame at *O*): $\Delta x_{OA} = 0$, $\Delta y_{OA} = 0$, $\Delta z_{OA} = -l$. The axial force resultant *N*, the bending moment resultants $M_y$, $M_z$ and the torsion moment resultant $M_t$ at *A* are calculated as:

$$\begin{aligned}&M_y = m_{Ay} = m_y + l f_x,\ M_z = m_{Az} = m_z, \\ &N = f_{Ax} = f_x,\ M_t = m_{Ax} = m_x - l f_y\end{aligned} \tag{15}$$

$M_y$, $M_z$, *N* and $M_t$ of Eq. (15) are introduced in Eqs. (12) and (13), and the resulting $\sigma_{\max}$ , $\tau_{\max}$ are further substituted into the limit-form of Eq. (11) where the equivalent stress becomes the allowable stress: $\sigma_{eq} = \sigma_a$. The resulting equation enables to perform any of the following three possible evaluations: (1) check the maximum stresses for known load and hinge properties to ensure it is smaller than

$\sigma_a$; (2) determine (one component of the) external load $\boldsymbol{f}$ with specified hinge geometry and material properties; or (3) size the hinge (*i.e*. determine one geometric parameter) for given external load and material properties.

Section 4 includes a case study that investigates the maximum force and resulting displacements of a 3D flexible hinge that is attached to a rigid arm by using the stress-based analytical model derived in this section.

## 4. ANALYTICAL-MODEL SIMULATION

The analytical models formulated in section 3 are applied in this section to comprehensively investigate the qualitative and quantitative relationships between the flexible hinge geometry and its compliances. A similar study is performed to identify the influence of the hinge geometric parameters on the maximum loads and resulting displacements of a simple flexible hinge mechanism when the stress limitations are being considered.

### 4.1. Compliances

We are studying here the relationships between the hinge geometric parameters and the various analytical compliances. Compliance changes result from individual scaling (when one parameter varies at a time), as well as from uniform scaling (when all parameters vary by means of the same scale factor). Coordinate coupling is also discussed in the context of parameter scaling. The section also includes a parameter study of the piston-motion stiffness and of the serial-connection flexible hinge compliances.

#### 4.1.1. Parameter scaling and coordinate coupling

a) *Individual-parameter scaling*. The analytical compliance model is utilized here to study the variations in the compliances of the matrix $\boldsymbol{C}_O$ that are produced by changes in the flexible hinge geometric parameters $R_1$, $R_2$, $R_3$ $d$, $l$ and $g$ (which are identified in Fig. 2). It is qualitatively reasonable to assume that larger radii $R_1$, $R_2$, $R_3$ of the circular-axis segments, accompanied by longer straight-axis segments, will generate flexible hinges with larger compliances. Similarly, smaller cross-section diameters $d$ should have the same effect on compliances.

We have performed a thorough analysis of the dependency of all individual compliances on each of the geometric parameters. A set of constant parameters were used as a baseline, namely: $R_1$ = 20 mm, $R_2$ = 35 mm, $R_3$ = 50 mm, $d$ = 2 mm, $l$ = 8 mm, $g$ = 4 mm, $E = 1.2\cdot10^{11}$ N/m$^2$ and $\mu$ = 0.3. These values were also used in all subsequent analysis in section 4.1.1. Each geometric parameter was varied within a range around its constant baseline value while keeping all other parameters constant. This step served at detecting the monotony trend in compliances. Once the increasing/decreasing nature of a compliance with respect to a geometric parameter was established, a compliance ratio was formulated where the denominator is the minimum-value compliance and the denominator is the variable compliance. The following ratios can be formed of the total 21 compliance ratios:

$$r_{11} = \frac{C_{11}}{C_{11,\min}};\ r_{15} = \frac{C_{15}}{C_{15,\min}};\ r_{16} = \frac{C_{16}}{C_{16,\min}};\ r_{26} = \frac{C_{26}}{C_{26,\min}}, \tag{16}$$

where $C_{11}$, $C_{16}$ and $C_{26}$, are translation compliances while $C_{15}$ is a hybrid compliance (it connects the translation $u_y$ to the moment $m_x$). The study confirmed the variation expectations just formulated, as illustrated in Fig. 8, where the four compliance ratios of Eq. (16) are plotted in terms of $R_1$, $R_2$, $d$ and $l$. Similar trends are displayed by all other compliances whose plots are not included here. While the compliance variation with $d$ is strongly nonlinear (as expected, given that $d^3$ is the largest power in all compliances), alterations in the radii $R_1$, $R_2$ and $R_3$ result in quasi-linear changes in compliances, while the compliance variations with the out-of-plane connecting segment length $l$ is linear. It was also noticed that variations in $g$, even large ones, do not sensibly affect the compliances, which remain quasi constant.

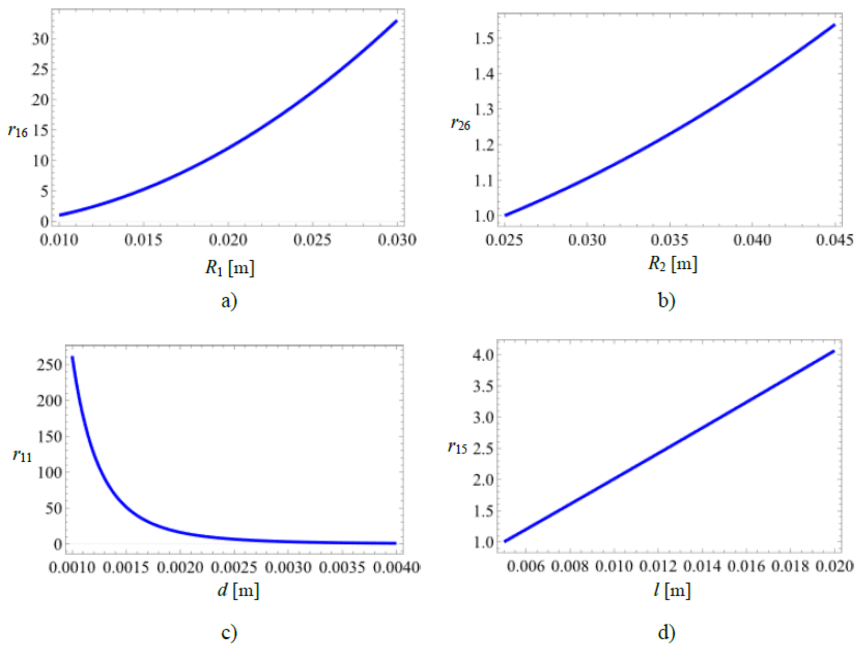


Fig. 8 – Compliance ratio plots in terms of: a) inner radius $R_1$; b) middle radius $R_2$; c) diameter $d$; d) out-of-plane segment length $l$.

b) *Comparison between direct compliances*. Direct compliances express relationships between load and displacement components corresponding to the same DOF; they are located on the main diagonal of the hinge compliance matrix $\boldsymbol{C}_O$. The emphasis here is to compare the direct translation compliances $C_{11}$, $C_{22}$, $C_{66}$, as well as the direct rotation compliances $C_{33}$, $C_{44}$, $C_{55}$ between themselves. Simulation demonstrated that $C_{66} > C_{22} > C_{11}$ and $C_{44} > C_{55} > C_{33}$. Given these compliance relationships, the following ratios:

$$r_{t1} = \frac{C_{22}}{C_{11}};\ r_{t2} = \frac{C_{66}}{C_{11}};\ r_{r1} = \frac{C_{44}}{C_{33}};\ r_{r2} = \frac{C_{55}}{C_{33}}, \tag{17}$$

that are larger than 1 (one) were utilized (where "*t*" stands for translation and *r* for rotation) and plotted against the six geometric parameters. It was noted that all ratios are monotonically increasing or decreasing over their variables ranges. To illustrate this, Fig. 9 graphs the ratios $r_{t2}$ and $r_{r2}$ in terms of the inner radius $R_1$.

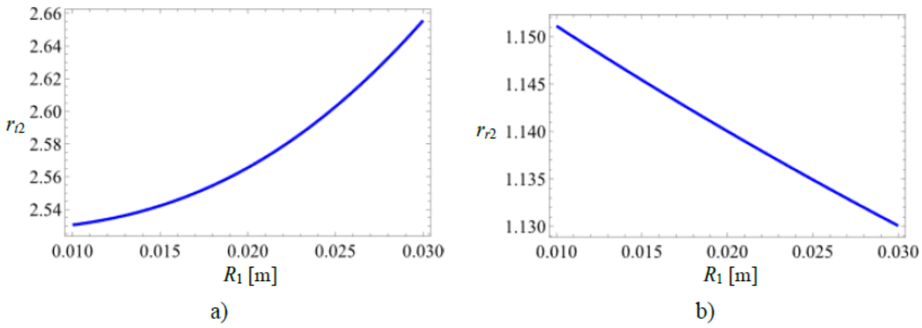


Fig. 9 – Plots in terms of the inner radius $R_1$ of: a) translation compliance ratio $r_{t2}$; b) rotation compliance ratio $r_{r2}$.

c) *Coordinate coupling*. An important aspect, also studied here, is the coupling between the various loads and displacements, which can be established by inspecting the form of the hinge compliance matrix $\boldsymbol{C}_O$, specifically the off-diagonal elements. For instance, a zero value in row *i* and column *j* of $\boldsymbol{C}_O$ indicates no coupling between the load (force or moment) applied in position *j* of the load vector $\boldsymbol{f}$ and the resulting displacement (translation or rotation) in position *i* of the displacement vector $\boldsymbol{u}$. Conversely, a non-zero compliance value at position (*i*, *j*) in $\boldsymbol{C}_O$ points at coupling between these load and displacement components. Both the analytical equation of $\boldsymbol{C}_O$ and the thorough numerical/graphical analysis performed in this section resulted in the following particular form of the hinge compliance matrix:

$$\boldsymbol{C}_O = \begin{bmatrix} C_{11} & C_{12} & 0 & C_{14} & C_{15} & C_{16} \\ C_{12} & C_{22} & C_{23} & C_{24} & C_{25} & 0 \\ 0 & C_{23} & C_{33} & 0 & 0 & 0 \\ C_{14} & C_{24} & 0 & C_{44} & 0 & 0 \\ C_{15} & C_{25} & 0 & 0 & C_{55} & C_{56} \\ C_{16} & 0 & 0 & 0 & C_{56} & C_{66} \end{bmatrix}. \quad (18)$$

As Eq. (18) shows, the zero matrix elements indicate that there is no coupling between:

– the moment $m_z$ and the displacement $u_x$;

– the force $f_z$ and the displacement $u_y$;

– the moments $m_x$, $m_y$, the force $f_z$ – on one hand – and the rotation $\theta_z$ – on the other hand.

– the moment $m_y$, the force $f_z$ – on one hand – and the rotation $\theta_x$ – on the other hand.

d) *Uniform scaling*. It is also of interest to investigate how scaling all geometric parameters by means of the same factor affects the deformation capacity of the flexible hinge. For a scaling factor *s*, the defining (variable) geometric parameters are expressed as:

$$R_1 = sR_{10},\ R_2 = sR_{20},\ R_3 = sR_{30},\ d = sd_0,\ l = sl_0,\ g = sg_0, \quad (19)$$

where $R_{10}$, $R_{20}$, $R_{30}$, $d_0$, $l_0$ and $g_0$ are the base (constant) values previously specified in this section 4.1.1.

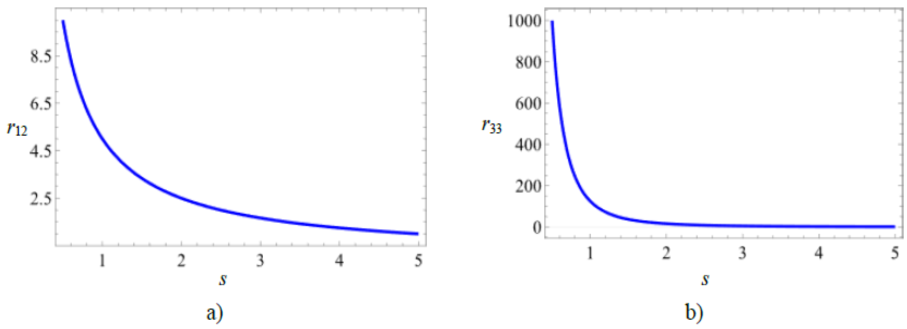


Fig. 10 – Scale-factor-dependent plots of compliance ratio: a) $r_{12}$; b) $r_{33}$.

It was noted that the compliances decrease when *s* increases, which indicates that the weight of scaling the diameter *d* is prevalent over the other dimensions scaling. Ratios similar to those defined in Eq. (16) can be formed, of which the following ones are used here:

$$r_{12} = \frac{C_{12}}{C_{12,\min}};\ r_{33} = \frac{C_{33}}{C_{33,\min}}, \tag{20}$$

to illustrate the compliances variation with $s$ – see Fig. 10. For $s$ ranging in the [0.5; 5] interval, compliances are minimum for $s$ = 5. The maximum value of $r_{12}$ is 10, while the maximum value of $r_{33}$ is 1,000.

#### 4.1.2. Piston-motion stiffness

The piston-motion stiffness $k_z$ of Eq. (9) was studied in terms of the flexible hinge geometric parameters. The following constant (base) values of parameters were used: $R_1$ = 0.02 m, $R_2$ = 0.035 m, $R_3$ = 0.05 m, $d$ = 0.004 m, $l$ = 0.008 m, $g$ = 0.004 m, $E = 2.61 \cdot 10^9$ N/m$^2$ and $\mu$ = 0.35 to obtain the graphs of Fig. 11. As expected, the stiffness becomes smaller with the radii $R_1$ and $R_2$ increasing and grows larger with larger cross-section diameters $d$, as illustrated in Fig. 11. It was noted that $k_z$ is constant when the outer radius $R_3$ varies, whereas changes in the gap $g$ and out-of-plane offset length $l$ results in very small $k_z$ variations.

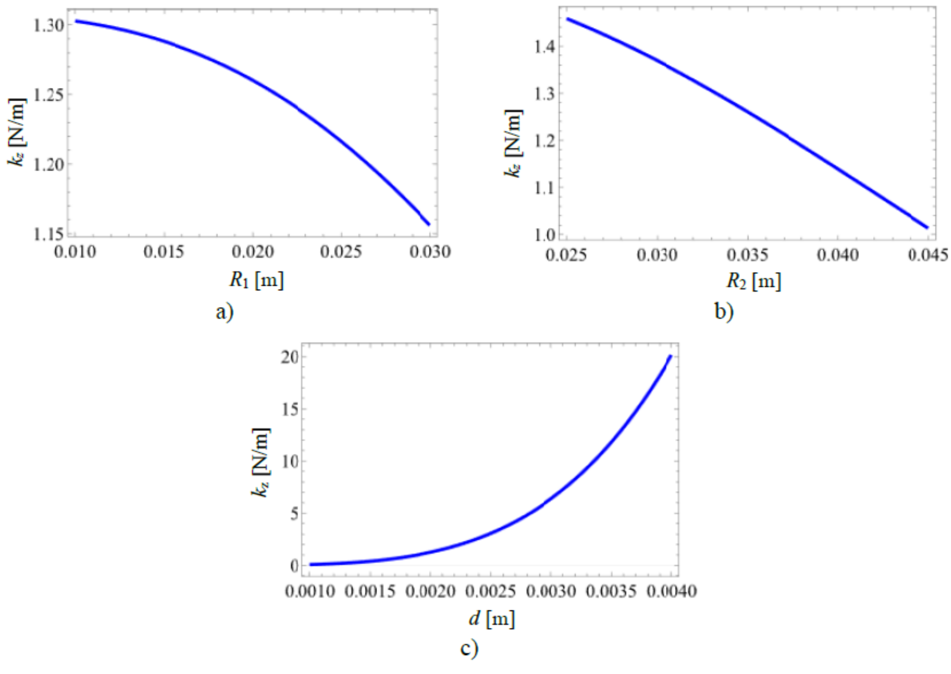


Fig. 11 – Piston-motion stiffness plots in terms of: a) inner radius $R_1$; b) middle radius $R_2$; c) diameter $d$.

### 4.1.3. NUMBER OF HINGE UNITS IN SERIES CONNECTION

The compliance matrix of the device that serially combines several identical flexible hinges is expressed in Eq. (10). It is meaningful to check how the compliance matrix of the series hinge device is affected by the length $l_c$ of the rigid link connecting two adjacent hinge units. The following compliance ratios were formed and graphed in Fig. 12 and 13:

$$r_{11} = \frac{C_{11,2}}{C_{11}};\ r_{16} = \frac{C_{16,2}}{C_{16}};\ r_{22} = \frac{C_{22,3}}{C_{22}};\ r_{24} = \frac{C_{24,3}}{C_{24}}. \tag{21}$$

The additional subscripts 2 and 3 in the numerators of Eq. (21) represent devices that combine two and three flexible hinges, respectively; the denominator compliances define a single flexible hinge.

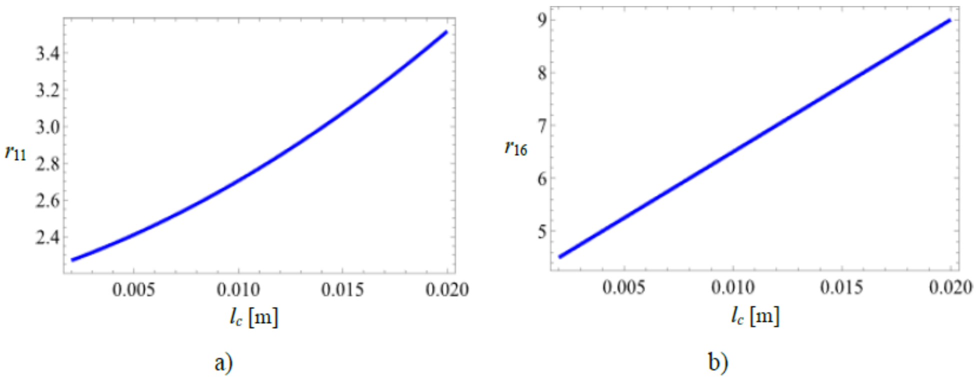


Fig. 12 – Plots comparing compliances of a two-unit hinge with one-unit hinge in terms of the connection segment length $l_c$: a) $r_{11}$; b) $r_{16}$.

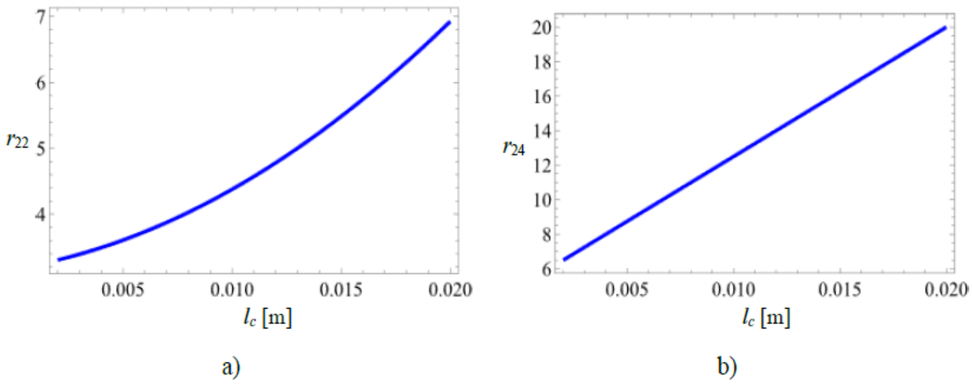


Fig. 13 – Plots comparing compliances of a three-unit hinge with one-unit hinge in terms of the connection segment length $l_c$: a) $r_{22}$; b) $r_{24}$.

As Figs. 12 and 13 indicate, the multiple-hinge devices are, evidently, more compliant than a single flexible hinge (all ratios are larger than one); also, as the figures indicate, the multiple-hinge devices become more flexible than the single hinge when $l_c$ increases. The four compliances in the ratios of Eq. (21) were the only ones changing. The other compliances, as it was noted from their plots (not included here), are constant with respect to $l_c$ variation – their corresponding ratios are equal to either 2 or 3.

### 4.2. Maximum loads and displacements of simple flexible hinge mechanism

The analytical compliance model developed in section 3.2 was applied to the simple mechanism of Fig. 14 that consists of a rigid arm connected to the 3D flexible hinge. The rigid arm is formed of three straight-axis segments that are aligned with the global Cartesian frame *Oxyz* placed at the moving end of the hinge (see Fig. 2). Assume that three forces $F_x$, $F_y$, $F_z$ are applied at the rigid arm end *B* along the *x*, *y*, *z* axes; assume also that the force magnitudes are defined in terms of a single (resultant) force *F* as:

$$\left.\begin{array}{l} F_x = c_x F,\; F_y = c_y F,\; F_z = c_z F \\ F = \sqrt{F_x^2 + F_y^2 + F_z^2} \end{array}\right| \;\rightarrow\; c_x^2 + c_y^2 + c_z^2 = 1. \tag{22}$$

Equation (22) indicates that the coefficients/fractions $c_x$, $c_y$, $c_z$ (whose magnitudes are less than < 1) are dependent.

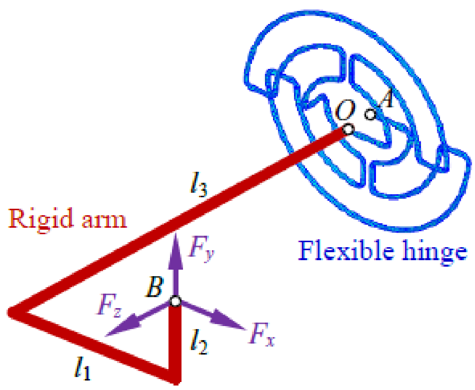


Fig. 14 – 3D rigid arm with flexible hinge and external load.

The force vector $\boldsymbol{f}_A$ at the fixed point *A* results in this case from the force vector $\boldsymbol{f}_B$ applied at *B* as:

$$\boldsymbol{f}_A = \boldsymbol{T}_{BA}\boldsymbol{f}_B = \boldsymbol{T}_{BA}\begin{bmatrix} c_x F & c_y F & 0 & 0 & 0 & c_z F \end{bmatrix}^T. \tag{23}$$

The translation matrix $[T_{BA}]$ is calculated as in *Appendix B* with the offsets (evaluated from $B$): $\Delta x_{BA} = -l_1$, $\Delta y_{BA} = -l_2$, $\Delta z_{BA} = -l_3 \ -l$. The components of $\boldsymbol{f}_A$ in Eq. (23) are all proportional to $F$. They enable to determine $M_y$, $M_z$, $N$ and $M_t$ similarly to Eq. (15) and eventually to obtain an equation of the form:

$$\sigma_a = cF_{\max}, \tag{24}$$

where the proportionality coefficient $c$ is provided in *Appendix B*. Equation (24) can be utilized to determine the maximum force $F_{\max}$, which enables to calculate the three force components at $B$ for different fractions. Eventually, the (maximum) force vector at $B$ is translated at the hinge end $O$ as:

$$\boldsymbol{f}_{\max} = \boldsymbol{T}_{BO}\boldsymbol{f}_{B,\max} = \boldsymbol{T}_{BO}\begin{bmatrix} c_x F_{\max} & c_y F_{\max} & 0 & 0 & 0 & c_z F_{\max} \end{bmatrix}^T, \tag{25}$$

which results in the maximum displacement vector at the same point:

$$\boldsymbol{u}_{\max} = \boldsymbol{C}_O \boldsymbol{f}_{\max}. \tag{26}$$

The offsets in $\boldsymbol{T}_{BO}$ are: $\Delta x_{BO} = -l_1$, $\Delta y_{BO} = -l_2$, $\Delta z_{BO} = -l_3$. Figures 15, 16, 17, 18 and 19 plot the changes in $F_{\max}$ and in several displacement components in terms of geometric parameters. The simulation plots used steel properties with $E = 2\cdot10^{11}$ N/m$^2$, $\mu = 0.3$, $\sigma_a = 280\cdot10^{11}$ N/m$^2$, as well as the following constant values: $R_1 = 0.01$ m, $R_2 = 0.035$ m, $R_3 = 0.05$ m, $d = 0.002$ m, $l = 0.008$ m, $g = 2d$, $l_1 = 0.08$ m, $l_2 = 0.05$ m, $l_3 = 0.12$ m, $c_x = 0.5$, $c_y = 0.5$ and $c_z = 0.707$ (from Eq. 22). As expected, the maximum displacement and/or rotation angles at the moving end of the flexible hinge increase with the radii, as illustrated in Figs. 15 and 16. Also confirming expectations are the plots of Fig. 17, which indicate that the maximum force increases and the maximum displacements decrease with the cross-section diameter increasing. The maximum force becomes larger while some displacements, such as $u_y$, become smaller when the length of the segment connecting the two hinge halves increases – see Fig. 18. Eventually, Fig. 19 depicts the variation of the maximum force and of $\theta_z$ with the force weight $c_x$; it can be seen that both output parameters display a non-monotonic variation since an increase in $c_x$ while keeping $c_y$ constant, leads to a decrease in $c_z$ based on the connection between the three force fractions. Overall, the parametric analysis indicates that the flexible hinge studied here can achieve maximum displacements of almost 0.07 m (see Fig. 15a) and rotation angles more than of $2\pi/3$ or 120° (as in Fig. 17b) while sustaining maximum forces of 80 N (such as in Fig. 17a).

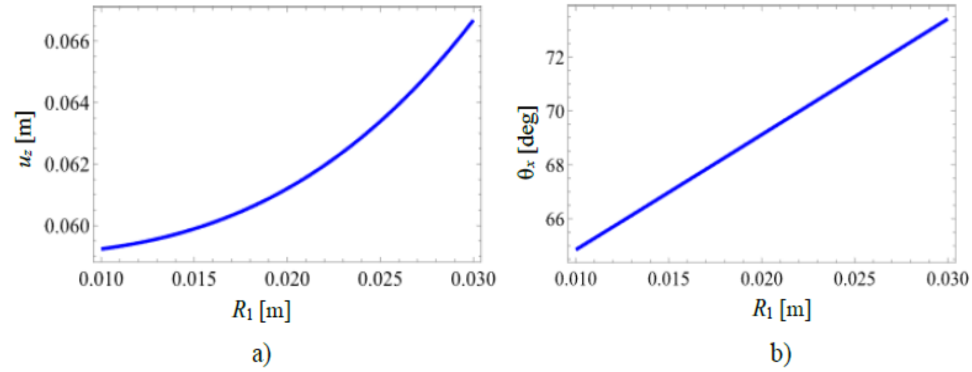


Fig. 15 – Plots in terms of inner radius $R_1$ for: a) displacement $u_z$; b) rotation angle $\theta_x$

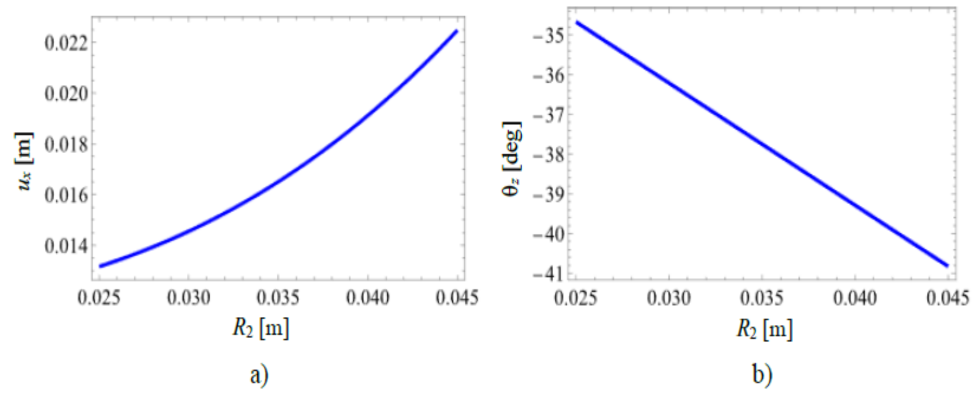


Fig. 16 – Plots in terms of middle radius $R_2$ for: a) displacement $u_x$; b) rotation angle $\theta_z$

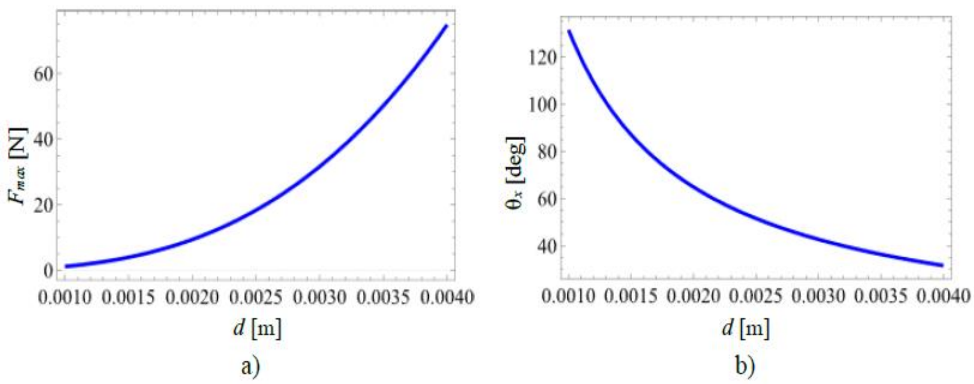


Fig. 17 – Plots in terms of diameter $d$ for: a) maximum force $F_{\max}$; b) rotation angle $\theta_x$

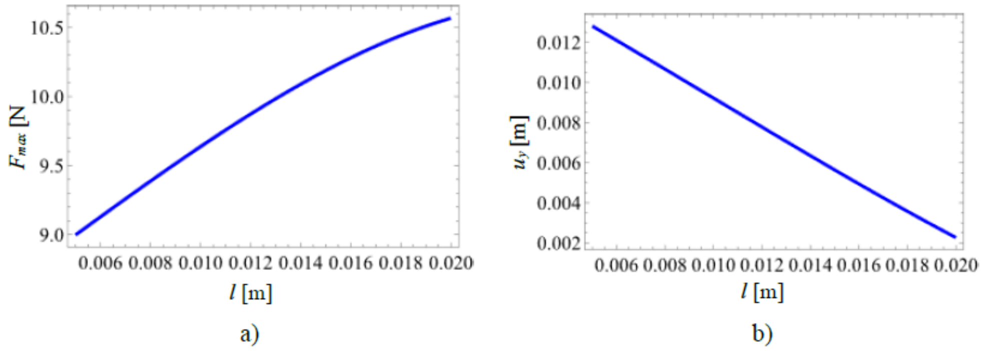


Fig. 18 – Plots in terms of offset length $l$ for: a) maximum force $F_{\max}$; b) displacement $u_y$

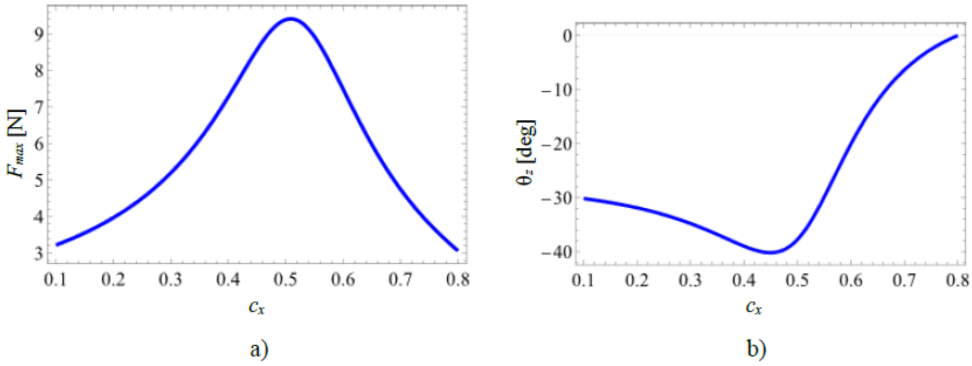


Fig. 19 – Plots in terms of force fraction $c_x$ for: a) maximum force $F_{\max}$; b) rotation angle $\theta_z$

*Remark*. It should be noted that some of the maximum displacements or rotations registered at the hinge free end in Figs. 15 through 19, while large (see the angle $\theta_x$ of approximately 120° in Fig. 17b for instance), are still within the linear-model confines. A simple back-of-the-envelope calculation can prove this point. Consider that the flexible hinge is unwound in the shape of a straight fixed-free member of total length $L$ and constant diameter $d$. A torque $m_x$ applied at this bar's free end produces the rotation $\theta_x$ at the same point, which is evaluated based on the small-deformation, linear torsion theory as:

$$\theta_x = \frac{m_x L}{G I_p} = \left(\frac{2 I_p \tau_a}{d}\right)\left(\frac{L}{G I_p}\right) = \frac{2\tau_a l}{G d} = \frac{4(1+\mu)\tau_a L}{E d}. \tag{27}$$

For $R_1 = 0.01$ m, $R_2 = 0.035$ m, $R_3 = 0.05$ m, the bar length is calculated by adding all the hinge segment lengths, which yields approximately $L = 0.78$ m. When $d = 0.001$ m and the material is steel with $E = 2{\cdot}10^{11}$ N/m$^2$, $\mu = 0.3$ and the allowable shear stress $\tau_a = 120{\cdot}10^{11}$ N/m$^2$, the angle of Eq. (27) is around 140°, which is still slightly larger than the 120º maximum value of Fig. 17b. However, both the shear strain and the corresponding stress are within the bounds of the small-deformation, linear-model theory. Similar simple calculations can easily be performed to reveal large displacements that are associated with bending of the fixed-free straight beam, which confirm the other maximum displacements/ rotations identified in Figs. 15b, 16b, 18b and 19b.

## 5. CONCLUSIONS

The paper studies a new three-dimensional flexible hinge that is capable of large displacements in precision positioning/manipulation mechanisms where realization of extended spatial workspaces is required. The hinge is designed in a modular, folded and stacked manner by serially connecting a large number of circular- and straight-axis segments in two parallel planes. The analytical compliance matrix of the simplified-geometry configuration is derived to characterize the overall elastic response of the hinge, as well as to predict the maximum load that can be applied to the hinge and the resulting displacements based on the allowable stresses. The validity of the theoretical model is verified with finite element simulation and experimental testing of a hinge specimen. The 3D hinge displays a linear characteristic over a wide displacement range, which further justifies the validity of the linear, small-deformation compliance model formulated here. To aid design, the relationships between the hinge performance and the geometric parameter ranges are subsequently studied by utilizing the derived mathematical models.

***Acknowledgements.*** The authors would like to thank Mr. Daniel Min for his contribution with the CAD drawings, as well as to the Manufacturing Laboratory in the College of Engineering at University of Alaska Anchorage for fabricating the hinge specimens.

*Received on February 15, 2024*

## REFERENCES

1. PAROS, J.M., WEISBORD, L. *How to Design Flexure Hinges*, Machine Design, November, pp. 151–156, 1965.
2. SMITH, S.T., BADAMI, V.G., DALE, J.S., XU, Y., *Elliptical Flexure Hinges*, Precision Engineering, **68**, pp. 1474–1483, 1997.
3. SMITH, S.T., *Flexures: Elements of Elastic Mechanisms*, Gordon & Breach, Amsterdam, 2000.
4. LOBONTIU, N., *Compliant Mechanisms: Design of Flexure Hinges*, 2nd ed., CRC Press, Boca Raton, 2020.
5. LI, L., ZHANG, D., QU, H., WANG, Y., *Generalized Model and Configuration Design of Multiple-Axis Flexure Hinges*, Mechanism and Machine Theory, **169**, pp. 104677–1-27, 2022.
6. LING, M. *et al.*, *Compliance and Precision of General Notch Hinges Using a Discrete-Beam Transfer Matrix*, Precision Engineering, **82**, pp. 233–250, 2023.

7. SCHOTBORG, W.O. *et al*. *Dimensionless Design Graphs for Flexure Elements and a Comparison Between Three Flexure Elements*, Precision Engineering, **29**, pp. 41–47, 2005.
8. CHEN, G. *et al*., *A Generalized Model for Conic Flexure Hinges*, Review of Scientific Instruments, **80**, pp. 055106 – 1-10, 2009.
9. HARFENSTELLER, F., HENNING, S., ZENTNER, L., HUSUNG, S., *Modeling of Corner-Filleted Flexure Hinges under Various Loads*, Mechanism and Machine Theory, **175**, pp. 104937 –1-11, 2022.
10. LINB, S., ERBE, T., ZENTNER, L., *On Polynomial Flexure Hinges for Increased Deflection and an Approach for Simplified Manufacturing*, 13th World Congress in Mechanism and Machine Science, Guanajuato, Mexico, 19–25 June, 2011.
11. LI, Q., PAN, C., XU, X., *Closed-Form Compliance Equations for Power-Function-Shaped Flexure Hinge Based on Unit-Load Method*, Precision Engineering, **37**, pp. 135–145, 2013.
12. VALLANCE, R.R., HAGHIGHIAN, B., MARSH, E.R., *A Unified Geometric Model for Designing Elastic Pivots*, Precision Engineering, **32**, pp. 278–288, 2008.
13. WU, J. et al., *Modeling and Analysis of Conical-Shaped Notch Flexure Hinges Based on NURBS*, Mechanism and Machine Theory, **128**, pp. 560–568, 2018.
14. TIAN, Y., SHIRINZADEH, B., ZHANG, D., *Closed-Form Compliance Equations of Filleted V-Shaped Flexure Hinges for Compliant Mechanism Design*, Precision Engineering, **34**, pp. 408–418, 2010.
15. LI, L. et al., *Design, Modeling, and Analysis of Hybrid Flexure Hinges*, Mechanism and Machine Theory, **13**, pp. 300–316, 2019.
16. WEI, H., et al., *Analytical Modelling and Experiments for Hybrid Multiaxis Flexure Hinges*, Precision Engineering, **76**, pp. 294–304, 2022.
17. LEE, V., ZIEGERT, J., *Hybrid Bi-Directional Flexure Joints*, Proceedings of ASPE 2007 Annual Meeting, Dallas, Texas, October 14–19, 2007.
18. SHUSHENG, B., SHANSHAN, Z., XIAOFENG, Z., *Dimensionless Design Graphs for Three Types of Annulus-Shaped Flexure Hinges*, Precision Engineering, **34**, pp. 659–666, 2010.
19. RAD, F.P., *et al*., *Analytical Compliance Analysis and Finite Element Verification of Spherical Flexure Hinges for Spatial Compliant Mechanisms*, Mechanism and Machine Theory, **101**, pp. 168–180, 2016.
20. LI, J., LIU, H., ZHAO, H., *A Compact 2-DOF Piezoelectric-Driven Platform Based on "Z-Shaped" Flexure Hinges*, Micromachines, **8**, *8*, pp. 245 – 1-14, 2017.
21. ABEDI, K. *et al*., *Design and Analysis of a 2-DOF Compliant Serial Micropositioner Based on "S-Shaped" Flexure Hinge*, Precision Engineering, **83**, pp. 228–236, 2023.
22. BILANCIA, P., BERSELLI, G., *An Overview of Procedures and Tools for Designing Nonstandard Beam-Based Compliant Mechanisms*, Computer Aided Design, **1**, pp. 103001 – 1-19, 2021.
23. QIU, L. *et al*., *Research on the Line-Arc-Line Constant-Torque Flexure Hinge (LAL-CTFH) Based on Improved Pseudo-Rigid-Body Model (PRBM)*, Mechanism and Machine Theory, **174**, pp. 104878 – 1-12, 2002.
24. CAO, L. *et al*., *Topology Optimization of Efficient and Strong Hybrid Compliant Mechanisms Using a Mixed Mesh of Beams and Flexure Hinges with Strength Control*, Mechanism and Machine Theory, **121**, pp. 213–227, 2018.
25. LOBONTIU, N., HUNTER, J., KEEFE, J., WESTENSKOW, J., *Tripod Mechanisms with Novel Spatial Cartesian Flexible Hinges*, Mechanism and Machine Theory, **167**, pp. 104521–104537, 2022.
26. LOBONTIU, N., HUNTER, J., ROBLES, B., *New 3D Cartesian Flexible Hinge and Tripod Mechanisms: Stress-Based Maximum Load and Displacement with Compliance Model*, The Romanian Journal of Technical Sciences: Applied Mechanics, **67**, *1*, pp. 43–59, 2022.
27. WITTRICK, W.H., *The Theory of Symmetrical Crossed Flexure Pivots*, Australian Journal of Science Research, **1**, *2*, pp. 121–134, 1948.

28. WEINSTEIN, W.D., *Flexure-Pivot Bearings*, Machine Design, **37**, *16*, pp. 136–145, 1965.
29. KANG, D., GWEON, D., *Analysis and Design of a Cartwheel-Type Flexure Hinge*, Precision Engineering, **37**, pp. 33–43, 2013.
30. MERRIAM, E.G., HOWELL, L.L., *Lattice Flexures: Geometries for Stiffness Reduction of Blade Flexures*, Precision Engineering, **45**, pp. 160–167, 2016.
31. PAN, A.J. *et al*., *Design and Analyze of Flexure Hinges Based on Triply Periodic Minimal Surface Lattice*, Precision Engineering, **68**, pp. 338–350, 2021.
32. GUHA, K., *et al*., *Novel Analytical Model for Optimizing the Pull-In Voltage in a Flexured Mems Switch Incorporating Beam Perforation Effects*, Solid State Electronics, **137**, pp. 85–94, 2017.
33. PENG, J., *et al*., *Design and Investigation of a Sensitivity-Enhanced Fiber Bragg Sensor for Micro-Strain Measurement*, Sensors and Actuators A: Physical, **285**, pp. 437–447, 2019.
34. KASHIAP, R., BAISHYA, S., TAYE, J., *Design and Simulation of a Compact Low-Stiffness Mems-Gate for Suspended-Gate Mosfet*, International Journal of Advancements in Technology, **5**, *2*, pp. 126–136, 2014.
35. FANG, Y.J., MUKHERJEE, T., FEDDER, G.K., *Si-CMOS Dual Mass Resonator for Extracting Mass and Spring Variations*, 2013 IEEE 26th International Conference on Micro Electro Mechanical Systems (MEMS), pp. 657–660, 2013.
36. LOBONTIU. N., WIGHT-CRASK, J., KAWAGLEY, C., *Straight-Axis Folded Flexure Hinges: In-Plane Elastic Response*, Precision Engineering, **57C**, pp. 54–63, 2019.
37. QIU, L. *et al*., *Design and Stiffness Analysis of a Pitch-Varying Folded Flexure Hinge (PFFH)*, Mechanism and Machine Theory, **157**, pp. 1–13, 2021.
38. LOBONTIU, N. *et al*., *A Compact Three-Dimensional Two-Layer Flexible Hinge*, Machines, **11**, 825, https://doi.org/10.3390/machines 11080825, 2023.

# APPENDICES

**Appendix A** *Translation and rotation matrices*

$$\boldsymbol{T}_{OO_i}^{(i)}=\begin{bmatrix}1&0&0&0&0&0\\0&1&0&0&0&0\\\Delta y_i&-\Delta x_i&1&0&0&0\\0&\Delta z_i&0&1&0&-\Delta y_i\\-\Delta z_i&0&0&0&1&\Delta x_i\\0&0&0&0&0&1\end{bmatrix}\tag{A1}$$

$$\boldsymbol{R}^{(i)}=\boldsymbol{R}_{\psi}^{(i)}\boldsymbol{R}_{\theta}^{(i)}\boldsymbol{R}_{\varphi}^{(i)}\tag{A2}$$

$$\begin{gathered}\boldsymbol{R}_{\beta}^{(i)}=\begin{bmatrix}\boldsymbol{R}_{\beta}^{(i1)}&\boldsymbol{0}\\\boldsymbol{0}&\boldsymbol{R}_{\beta}^{(i1)}\end{bmatrix};\quad \boldsymbol{R}_{\beta}^{(i1)}=\begin{bmatrix}\cos\beta_i&\sin\beta_i&0\\-\sin\beta_i&\cos\beta_i&0\\0&0&1\end{bmatrix}\quad \text{with}\quad \beta=\psi \text{ or } \beta=\varphi\\ \boldsymbol{R}_{\theta}^{(i)}=\begin{bmatrix}\boldsymbol{R}_{\theta}^{(i1)}&\boldsymbol{R}_{\theta}^{(i2)}\\\boldsymbol{R}_{\theta}^{(i2)}&\boldsymbol{R}_{\theta}^{(i1)}\end{bmatrix};\quad \boldsymbol{R}_{\theta}^{(i1)}=\begin{bmatrix}1&0&0\\0&\cos\theta_i&0\\0&0&\cos\theta_i\end{bmatrix};\quad \boldsymbol{R}_{\theta}^{(i2)}=\begin{bmatrix}0&0&0\\0&0&\sin\theta_i\\0&-\sin\theta_i&0\end{bmatrix}\end{gathered}\tag{A3}$$

*Table A1*

Straight-axis segment lengths, offsets, and rotation angles

| Segment | $l$ | $\Delta x$ | $\Delta y$ | $\Delta z$ | $\varphi$ | $\theta$ | $\psi$ |
|---|---|---|---|---|---|---|---|
| 1 | $R_1$ | 0 | 0 | 0 | 0 | 0 | 0 |
| 3 | $R_2\sin\alpha_2 - R_1\sin\alpha_1$ | $R_1\cos\alpha_1$ | $R_1\sin\alpha_1$ | 0 | $\pi/2$ | 0 | 0 |
| 5 | $R_3 - R_2$ | $R_2$ | 0 | 0 | 0 | 0 | 0 |
| 8 | $R_3 - R_2$ | $-R_3$ | 0 | 0 | 0 | 0 | 0 |
| 10 | $R_2\sin\alpha_2 - R_1\sin\alpha_1$ | $-R_2\cos\alpha_2$ | $R_2\sin\alpha_2$ | 0 | $-\pi/2$ | 0 | 0 |
| 12 | $l$ | $-R_1$ | 0 | 0 | $\pi/2$ | $-\pi/2$ | $\pi/2$ |
| 13 | $R_1$ | $R_1$ | 0 | $-l$ | $\pi$ | 0 | 0 |

*Table A2*

Circular-axis segment center angles, offsets, and rotation angles ($\Delta z = 0$, $\theta = 0^o$, $\psi = 0^o$)

| Segment | $\alpha$ | $\Delta x$ | $\Delta y$ | $\varphi$ |
|---|---|---|---|---|
| 2 | $\cos^{-1}[g/(2R_1)]$ | $R_1$ | 0 | $\pi/2$ |
| 4 | $\cos^{-1}[g/(2R_2)]$ | $R_1\cos\alpha_1$ | $R_2\sin\alpha_2$ | $\pi/2 + \alpha_2$ |
| 6 | $\pi/2$ | $R_3$ | 0 | $\pi/2$ |
| 7 | $\pi/2$ | 0 | $R_3$ | $\pi$ |
| 9 | $\cos^{-1}[g/(2R_2)]$ | $-R_2$ | 0 | $-\pi/2$ |
| 11 | $\cos^{-1}[g/(2R_1)]$ | $-R_1\cos\alpha_1$ | $R_1\sin\alpha_1$ | $3\pi/2 - \alpha_1$ |

## Appendix B

$$c=\sqrt{\left[\left(\frac{32}{\pi d^3}\right)\sqrt{\left[c_z\Delta x_{BA}-(\Delta z_{BA}-l)c_x\right]^2+\left(c_x\Delta y_{BA}-c_y\Delta x_{BA}\right)^2}+\frac{4c_x}{\pi d^2}\right]^2+ \atop +\frac{3\cdot 16^2\left[(\Delta z_{BA}-l)c_y-c_z\Delta y_{BA}\right]^2}{\left(\pi d^3\right)^2}} \tag{B1}$$